

# *J*-band Sythentic Spectral Fitting

July 30, 2015

In this chapter I describe in detail the process by which I implement an analysis routine to fit RSG sythetic spectra to observed data. The spectra cover the *J*-band, spectifically the  $1.16 - 1.22\mu\text{m}$  region, where there are various prominent spectral features. These spectral features, arising from elemental absorption, are compared in the observed and model spectra, where the  $\chi^2$ -statistic is calcualted to asses the goodness of fit for each model. The stellar parameters which are fit for in this analysis are global metallicity  $[Z]$ , effective temperature ( $T_{eff}$ ), microturbulence ( $\xi$ ) and surfance gravity ( $logg$ ). The observed spectra are fit with model spectra from a set of MARCS model atmospheres Gustafsson et al. (2008).

The wavelength range, over which to perform this analysis, is chosen based on the spectral appearance of the region. Typically, in the spectra of cool stars, dense molecular absorption fetuares dominate the spectrum which require high-resolution spectroscopy to distinguish individual features and derive stellar parameters Cunha et al. (2007); Davies et al. (2009a,b). However, in this small wavelength range, the absorption is dominated by well separaeted elemental absorption features from iron, magnesium, silicon and titanium. Therefore, the spectral resolution required in order to derive stellar paramters is significantly reduced. This means that this analyis can be preformed with a relatively small amount of telescope time using multi-object spectrographs like the *K*-band multi-object spectrograph (KMOS) or the multi-object spectrometer for infra-red exploration (MOSFIRE) and is therefore feasible for studies of red supergiant stars (RSGs) in external galaxies.

In addition to this, given the cool temperature of the outer layers of RSGs, the peak brightness of a typical RSG is  $\sim 1.1\mu\text{m}$ . Combining this with the fact that dust attenuation is significanlty lower in the near-IR, compared to the optical regime, RSGs are ideal candidates to be studied at large distances.

Previous implemenations of this analysis include that of Davies et al. (2010) and Gazak (2014). This implemenation includes aspects of both of these previous implementations and could be described as a hybrid of the two. I approach the implementation in a Bayesian manner which relies on good prior assumptions. Eventually this analysis routine will be made publicly available which should encourage the community to engage with these routines.

In the remainder of this chapter I first describe the model grids and how they are used in 0.1. I then describe the continuum fitting procedure in 0.2, and go on to detail the method for estimating the bestfit parameters in 0.3. The testing process which these procedures have underwent is described in ??, which also includes a comparison between the results produced using this implementation and those of the two previous implementations of the same analysis. Finally, I conclude the chapter in 0.6.

## 0.1 Model Grid

The model grids used in this analysis are based on model atmospheres computed from the MARCS model atmospheres project (Gustafsson et al., 2008). These model atmospheres are one-dimensional models (i.e. spherically symmetric) computed within local thermodynamic equilibrium (LTE). The MARCS models are particularly general and widely applicable to many different types of stars, however, for the atmospheres of RSGs these assumptions are known to break down (Freytag et al., 2002; Plez, 2010). Therefore, in order to accurately analyse the spectra of RSGs additional corrections must be made.

The models used for this analysis are computed with a mass of  $15M_{\odot}$ . The typical mass range of a RSG is within  $8\text{--}40M_{\odot}$  however, using this mass is applicable owing to the fact that altering the mass of these models affects only the extension (or geometrical thickness) of the models which does not change for red giants or supergiants (Davies et al., 2010).

To improve the accuracy of the model atmospheres non-LTE calculations have been performed for all elements which give rise to the diagnostic features within the wavelength range studied. The corrections are applied to iron, titanium, silicon and magnesium (Bergemann et al., 2012, 2013, 2014). Line profiles and non-LTE corrections are calculated using an updated version of the SIU code (Reetz, 1999; Bergemann et al., 2012).

The parameters of the resulting grid of model spectra are detailed in Table 1. The model spectra are at  $R = 10\,000$ , which is chosen to be significantly higher than the typical resolution of the observed spectra (i.e.  $R \sim 3000$ ). The sensitivity of each diagnostic line for a given free parameter is displayed in figures 1 through 4.

From an analysis of figures 1 and 2 it can be seen that the effect of increasing the metallicity of the models is similar to that of decreasing the surface gravity. It is therefore expected that a degeneracy exists between metallicity and surface gravity. This degeneracy is explored further in ??. The effect of varying the temperature of the models changes the relative strengths of the lines of different spectral species (e.g. iron to titanium). This is clearly distinguishable from all the effects of all other parameters. Increasing the microturbulence has the effect of increasing the equivalent widths of the strongest lines preferentially. Therefore, features arising from the same element will be most sensitive to this parameter.

**Table 1** *Model grid parameter space*

This is the grid which I currently have. What does the most modern grid we have look like?

Parameter	Abbreviation	Range	Increment
Global Metallicity	$[Z]$	+1.0 – -1.0	0.1 <i>dex</i>
Effective Temperature	$T_{eff}$	3400 – 4400	100 <i>K</i>
Log gravity	$logg$	+1.0 – -1.0	0.25 <i>dex</i>
Microturbulence	$\xi$	1.0 – 5.0	0.2 <i>km s<sup>-1</sup></i>

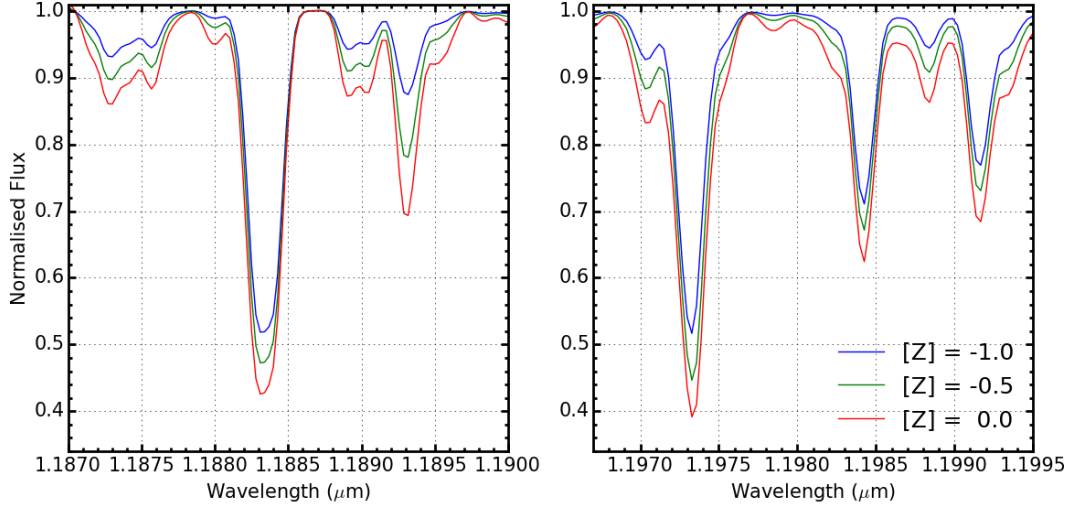


**Figure 1** *Three models where only the metallicity is varied. Five diagnostic lines are shown in two panels. Left: Fe I  $\lambda$  1.188285 and Ti I  $\lambda$  1.189289. Right: Fe I  $\lambda$  and Si I  $\lambda\lambda$  1.198419, 1.199157.*

This is illustrated by a comparison between the two strong iron lines in the left and right panel of Figure 4.

The current model grid is sufficient to explore the parameters for a typical RSG. However, when using this technique at larger distances, many different metallicity environments are encountered (e.g. I Zw 18 with  $Z = (1/32)Z_{\odot}$  (Vílchez and Iglesias-Páramo, 1998)). In order to study these extremely low-metallicity systems, the metallicity parameter space would need to be extended. The  $\alpha$ -to-iron ratio of these stars is taken to be that of the solar value and is not left as a free parameter in the models. This is applicable as young stars are known to have solar-like  $\alpha$ -to-iron ratios in different metallicity galaxies (see tables 3 and 4 in Davies et al., 2015, and references therein).

## 0.2 Continuum Fitting

Accurately matching the continuum levels in the models with that of the observed spectrum provides a base with which to anchor the diagnostic lines. An incorrectly

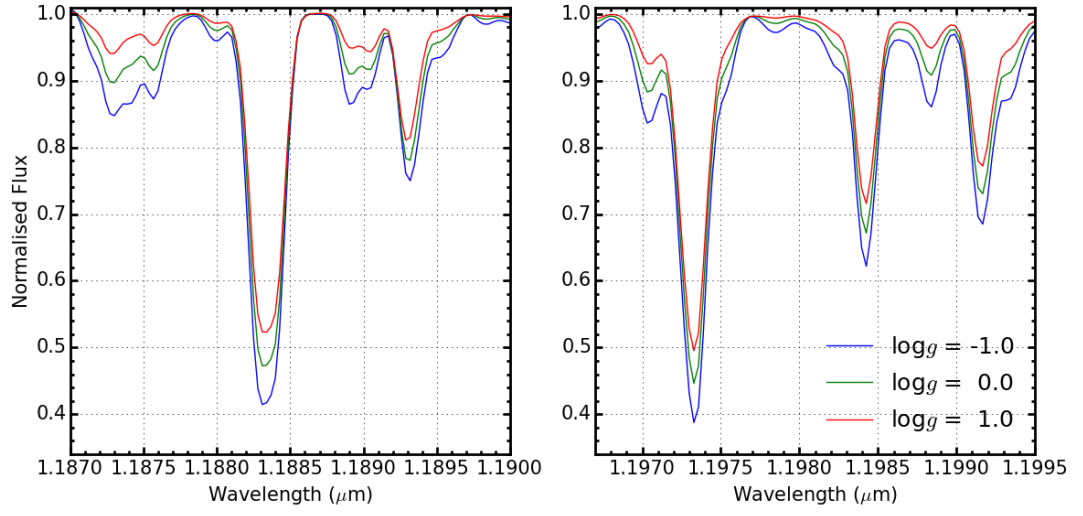


**Figure 2** *As in Figure 1 where however surface gravity is varied.*

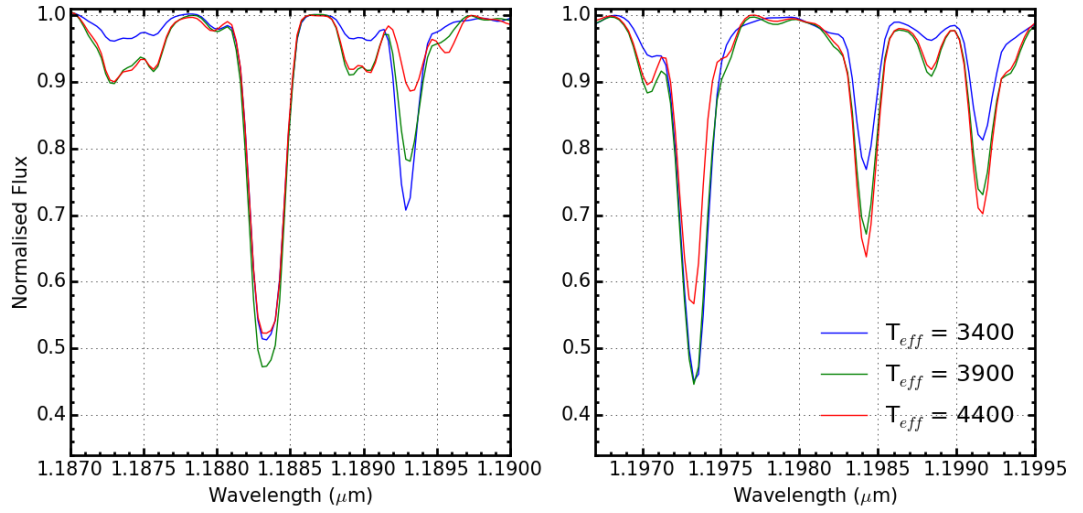


**Figure 3** *As in Figure 1 where however effective temperature is varied.*

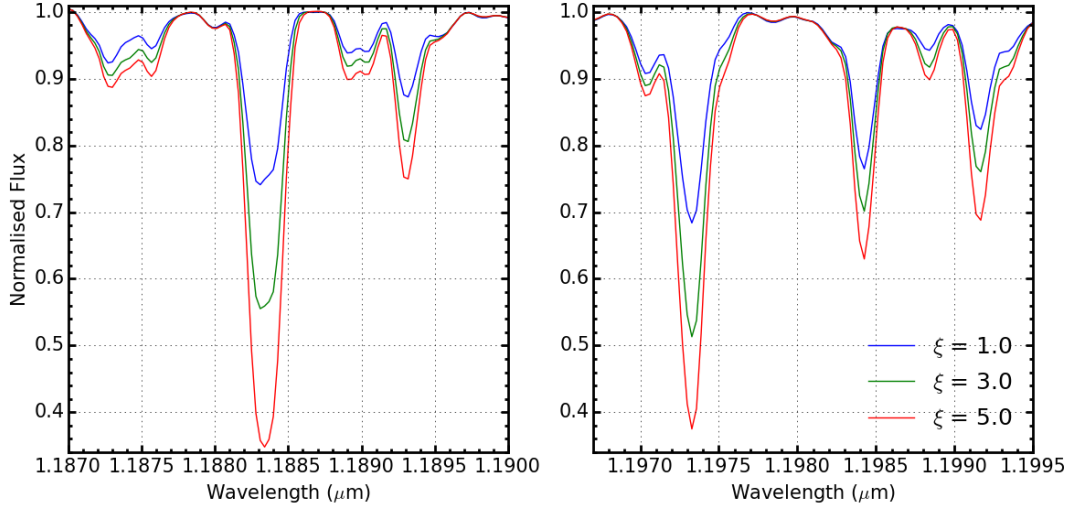


**Figure 4** *As in Figure 1 where however microturbulence is varied.*

placed continuum level would bias the analysis and result in the strength of the diagnostic lines being over or under estimated producing inaccurate stellar parameters.

There are many factors that effect the level of the continuum and continuum placement, including the resolution of the observations as well as the stellar parameters themselves. Therefore it is vital that when attempting to derive stellar parameters, in crowded regions such as this, the continuum placement is performed consistently and accurately. Intrinsically, when studying RSGs at medium resolution - owing to their cool atmospheres - there are many instances of blended spectral features. At this resolution the density of blended spectral features creates a pseudo-continuum which, in practice, is never at the true continuum level. Figure 5 illustrates the varying continuum levels for models where the resolution is varied and Figure 6 shows this affect when varying only the metallicity.

Given that it is impossible to know the true continuum level from any given observation, the scaling applied must be consistent between the models and observations. Scaling is required not only to match the levels of the continuum placement, but also to match the line strengths between the models and observations. Providing the treatment of the models and observations are consistent, the fact that the true continuum is never attained is not significant (Gazak et al., 2014). For this procedure to work effectively, the observed and model spectra should be at the same resolution, have a consistent wavelength calibration and have identical spectral sampling.

In order to account for differences in the spectral sampling of the observed and model spectra, each model spectrum is resampled onto the wavelength scale of the observations by means of a spline interpolation routine. The model spectrum is then degraded to the resolution of the observations by a convolution with

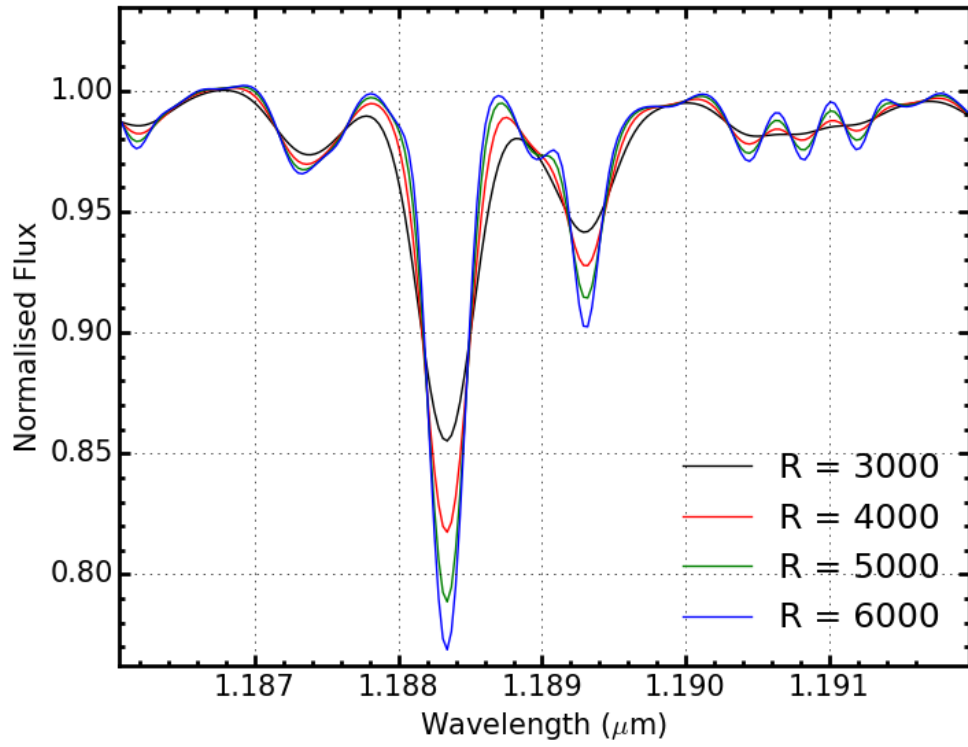


**Figure 5** *One model degraded to four different resolution values. This figure demonstrates the how the continuum level changes depending upon the resolution of the spectrum. We see at around 1.191μm at R = 3000 the continuum level is perturbed by blended lines.*

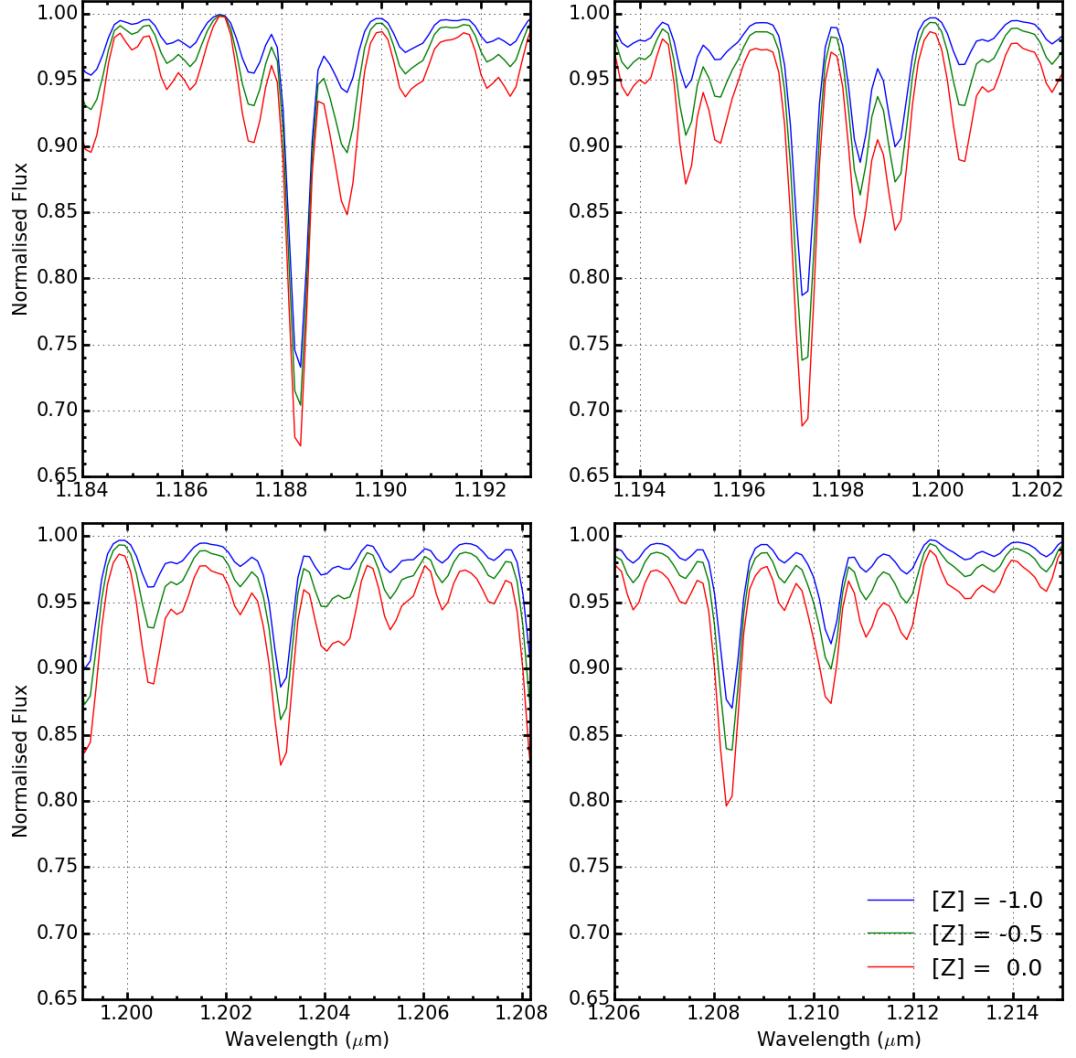


**Figure 6** *Three models where only the metallicity is varied. Each panel shows one or more diagnostic line. Metallicity of the model intrinsically affects the continuum level of the spectrum, such that at higher metallicities, there is greater departure from the true continuum level, which in the case of the models is 1.00.*

a Gaussian filter where the width of the Gaussian is defined by the observed resolution. The resolution of the KMOS observations is estimated using the KMOS/esorex pipeline from arc lamp exposures at the appropriate rotator angle for the observations. This is measured for each spectrograph and is assumed to be constant (to within  $\pm 100$ ) across individual IFU's as well as across the detector.

To ensure the spectra are on the same wavelength scale, the observed spectrum is cross-correlated with the model spectrum; a shift is then applied to the observed spectrum in order to minimise the cross-correlation matrix. This procedure is repeated until the shift between the observed and model spectra is less than  $0.1 \text{ pix}$ . Over this small wavelength range, one would not expect significant variations in the spectral resolution of the observations to perturb the cross-correlation.

Once the spectra have been correctly matched they are now suitable to be compared over the wavelength range  $1.165 - 1.215 \mu\text{m}$ . To estimate the amount of scaling required first I define the continuum width ( $cw$ ) as:

$$cw = \frac{\lambda}{R}, \quad (1)$$

where  $R$  is the resolution of the spectrum and  $\lambda$  is the wavelength at which the width is taken (in principle this wavelength varies across the spectrum, however, given our spectral window is sufficiently small, I assume  $\lambda = 1.20 \mu\text{m}$ ). The continuum width is essentially the resolution element of the spectrum at a wavelength of  $\lambda = 1.20 \mu\text{m}$  and defines the width in which we expect to find a combination of pixels from a spectral feature and a continuum point.

The model spectrum is divided into wavelength slices each of width  $cw \mu\text{m}$  and the maximum of each slice is taken. Using this array of maxima any major feature is systematically removed by rejecting data points more than  $3\sigma$  from the mean of the distribution. Figure 7 illustrates the width of these slices and how this technique removes prominent spectral features. In this figure blue points represent the boundaries between the slices of width  $cw \mu\text{m}$  and the maximum of each slice is shown in red.

The remaining data points ( $P_{cont}$ ) are used to derive an initial correction function ( $cf_1$ ) by fitting a third-order polynomial to the ratio of the model to observed continuum points, defined using the equation:

$$cf_1 = f\left(\frac{F_{mod}(P_{cont})}{F_{obs}(P_{cont})}\right) \quad (2)$$

where  $F_{mod}$  and  $F_{obs}$  are the flux in the model and observed spectrum respectively. The final correction function ( $cf_2$ ), a refinement of  $cf_1$ , is defined by removing any remaining outliers more than  $3\sigma$  from the mean of the correction function  $cf_1$ . This method assumes that over the small wavelength range considered,  $cf_1$  does not vary significantly from the mean and as such, any significant deviation is considered originating from a spectral feature or noise.



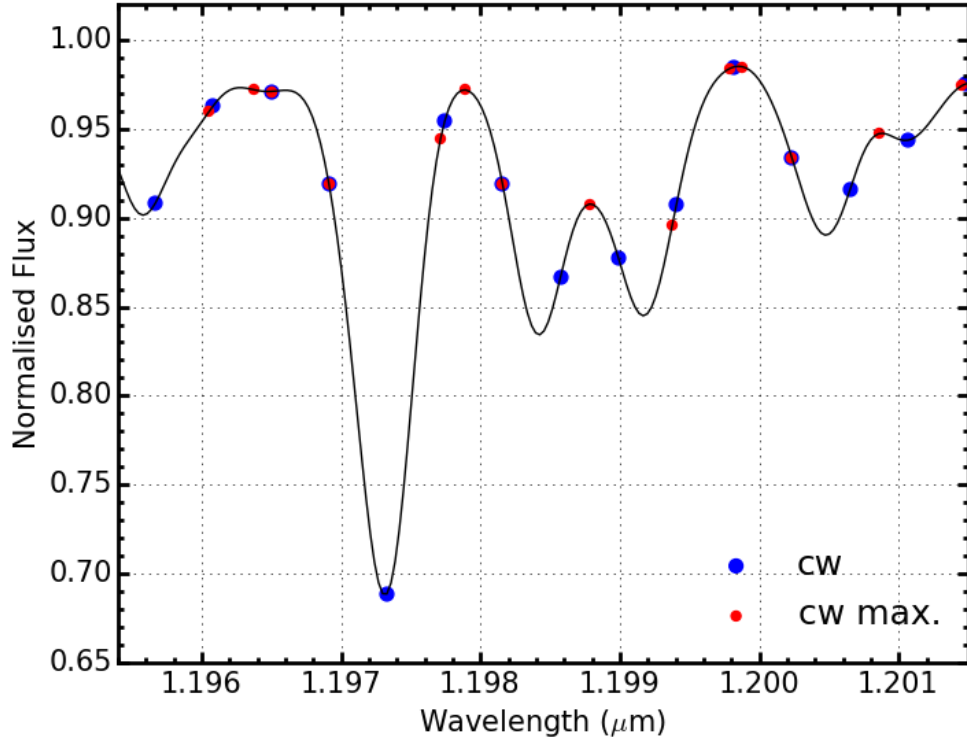


**Figure 7** *Illustration of the continuum width ( $cw$ ) and slicing the model spectrum into regions of  $cw\mu\text{m}$  is able to remove structure in order to fit the continuum. The solid black line shows an example of a model spectrum degraded to a resolution of 3000, blue points show the boundaries between the slices and red points show the maximum of each slice.*

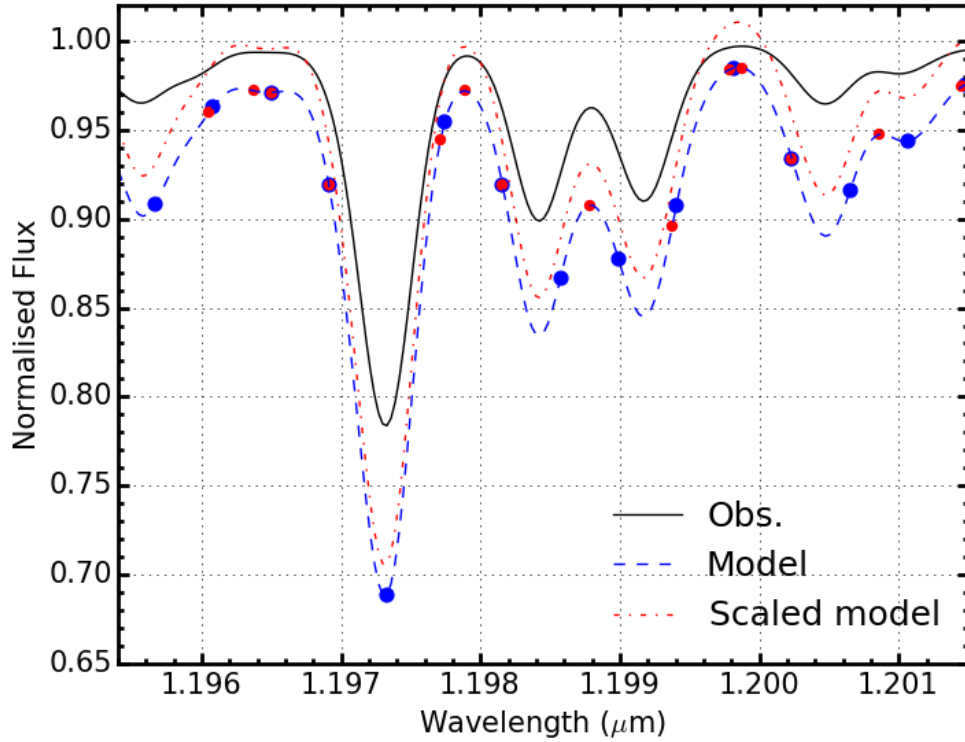


**Figure 8** *An example of how the continuum fitting procedure works using a model spectrum as an example observed spectrum (black solid line) and a separate model spectrum to match the level of the continuum. The dashed blue spectrum denotes the model spectrum before any scaling has taken place. The dot-dashed red spectrum denotes the model spectrum after the continuum fitting scaling has been applied. The red and blue points the edges of the slices made and maxima of these regions respectively.*

The final correction function,  $cf_2$ , is used to define the amount of scaling required for the model. Figure 8 shows how the continuum fitting process works using a model spectrum as the observed spectrum (black) and a second model spectrum (blue dashed) which is scaled to match the continuum level of the observed (red dot-dashed). It can be seen that the continuum placement of the example observed spectrum and that of the scaled model spectrum is well matched, even though the line strengths don't match well.

Alternative methods of continuum fitting are discussed in Davies et al. (2010) and Evans et al. (2011). These methods select pseudo-continuum pixels in the models based on ranking the model pixels and selecting a percentage of the pixels with the largest flux. Providing the pixels from the model are selected in this manner and not those in the observations, this is a reliable method with which to derive the continuum level as demonstrated by Davies et al. (2015).

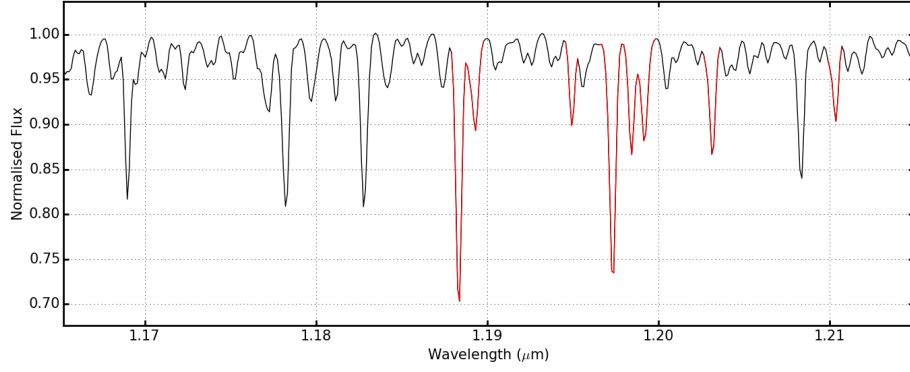


**Figure 9** *An example of a model spectrum, degraded and resampled to that of a typical observed spectrum (in this case NGC6822-RSG01), where the regions used to compute the  $\chi^2$  calculation is highlighted in red.*

### 0.3 Best Fit Parameters

Best fit parameters are calculated using a chi-squared minimisation approach. Each model is compared to the observed spectrum and the chi-squared statistic is calculated using the equation,

$$\chi^2 = \frac{1}{N_{pix}} \sum_i \frac{(O_i - M_i)^2}{\sigma^2}, \quad (3)$$

where  $N_{pix}$  is the number of pixels used and  $\sigma$  is determined by the S/N of the spectrum. This statistic is calculated over each of the diagnostic lines and here  $N_{pix}$  is the total number of pixels used to perform this calculation. Table 2 details the diagnostic lines used in this analysis. The amount of continuum included to compute the  $\chi^2$  is important to consider. If this wavelength range is too small, the wings of the lines will be neglected, which would discard vital information used to constrain the model parameters. However, if too much of the pseudo-continuum is included, the parameters could be biased by noise features in the observations or by inaccuracies within the models. For example, Gazak (2014) identify several spectral features present in the observed spectra which are missing in the model spectra. The regions which are used in the  $\chi^2$  calculation are highlighted red in figure 9. There are multiple cases where the diagnostic lines are sufficiently close together that, at  $R \sim 3000$ , the lines are not clearly separated. In these instances, the most appropriate course of action is to define the region where the  $\chi^2$  is computed over all of the lines in question and to deal with the region as a whole, as illustrated in Figure 9.

Each best fit parameter is estimated based on a weighted average, where the weights are determined by the  $\chi^2$  value of the model:

$$w = \exp(-\chi^2/2). \quad (4)$$

**Table 2** *Diagnostic lines*

Species	Line Centre
Fe I	1.188285
Fe I	1.197305
Si I	1.198419
Si I	1.199157
Si I	1.203151
Si I	1.210353
Ti I	1.189289
Ti I	1.194954
Mg I	
Mg I	

The average is performed using the 100 models with the lowest  $\chi^2$  value.

Errors on the parameters are determined by defining  $\Delta\chi^2 = \chi_{min}^2 + 3$ . The standard deviation of the models parameters for all models which have a  $\chi^2$  value within this range define the errors. For a purely Gaussian distribution the  $1\sigma$  deviation is  $\Delta\chi^2 = 2.3$ . However, assuming one of the diagnostic lines is only fit to within  $2\sigma$  while the rest being fit to within  $1\sigma$ , we obtain  $(n_l - 1) \times 1^2 + 1 \times 2^2 = n_l + 3$  where  $n_l$  is the number of lines used.

As mentioned previously (in 0.1) and as demonstrated in Davies et al. (2015) there exists a degeneracy between the effect of decreasing the metallicity and increasing the surface gravity of the models. To help break this degeneracy, I implement an addition gravity restraint. This works by calculating the luminosity of the observed star using near-IR photometry and the bolometric correction given in Davies et al. (2013). Having calculated the luminosity, the relationship,

$$L \propto \frac{M T_{eff}^4}{g}, \quad (5)$$

can be used to restrict the  $\log g$ - $T_{eff}$  parameter space using sensible limits for the mass of a RSG ( $8 \leq M/M_\odot \leq 40$ ). Where  $M$  is the mass of the star,  $T_{eff}$  is the effective temperature and  $g$  is the surface gravity of the star. These regions of parameter space are rejected from the analysis as unphysical.

## 0.4 Comparisons With Previous Implementations

To increase confidence in the accuracy and reliability of this implementation of the  $J$ -band synthetic spectral fitting routines, where applicable, these routines have been compared to the results based on previous implementations of this analysis.

To date, there are currently two other published implementations using medium resolution  $J$ -band spectra of RSGs to derive stellar parameters, that of Davies et al. (2010) (DFK10) and that of Gazak (2014). Both of these implementations are subtly different and use different assumptions to derive the stellar parameters. They are both broadly based on the same techniques used in this analysis,

**Table 3** *Average parameters for 10 RSGs in NGC 6822 using the DFK10 implementation and the implemetation discribed here*

Parameter	DFK10 Average	Patrick Average
[Z]	$-0.52 \pm 0.16$	
$T_{eff}$	$3887 \pm 55$	
$\log g$	$0.1 \pm 0.3$	
$\xi$	$3.9 \pm 0.5$	

however, the main differences between the two methods are that DFK10 uses just the line strenghts of the diagnostic lines to calculate the  $\chi^2$  statistic, while G14 uses the entire  $1.165 - 1.215 \mu\text{m}$  region (with some execeptions).

In the current implementation, the diagnostic lines themselves are used to calculate the  $\chi^2$  statistic. This is prefered to the two afformentioned techniques for the following reasons:

1. The models used in the analsyis are not perfect representations of RSG spectra. The line list which builds these spectra are known to be incomplete and the effect of including these wavelength regions within the  $\chi^2$  calculation could be to preturb the fit. G14 is very careful to exclude all known instances of missed lines within the models, however, this can not be assumed to be a complete consesus of missed lines.
2. Using the full line profile of the diagnostic lines provides information on the shape of the lines which using the line strength does not.

#### 0.4.1 DFK10

To date there have been several published articles using the DFK10 implemetation (Davies et al., 2010; Patrick et al., 2015; Davies et al., 2015). The original implemetation was updated and tested rigourously on VLT-XSHOOTER spectra of RSGs in the Magellanic clouds in Davies et al. (2015) and in Patrick et al. (2015) this was applied to KMOS spectra in NGC 6822. In this section we compare the analysis routine detailed above with that of DFK10 on the set of 10 RSG KMOS spectra in NGC 6822. Figure 10 shows the comparison of the output parmaters of the stars in this sample for the two analysis routines. This figure shows that the agreement between the two routines is acceptable for all stellar parameters. The mean of each of the parmeters is calculated in Table 3 and is shown to agree within the errors.

## 0.5 G14

The second implementation of the  $J$ -band analysis technique using  $J$ -band spectra of RSGs was that presented and rigorously tested in Gazak (2014). This

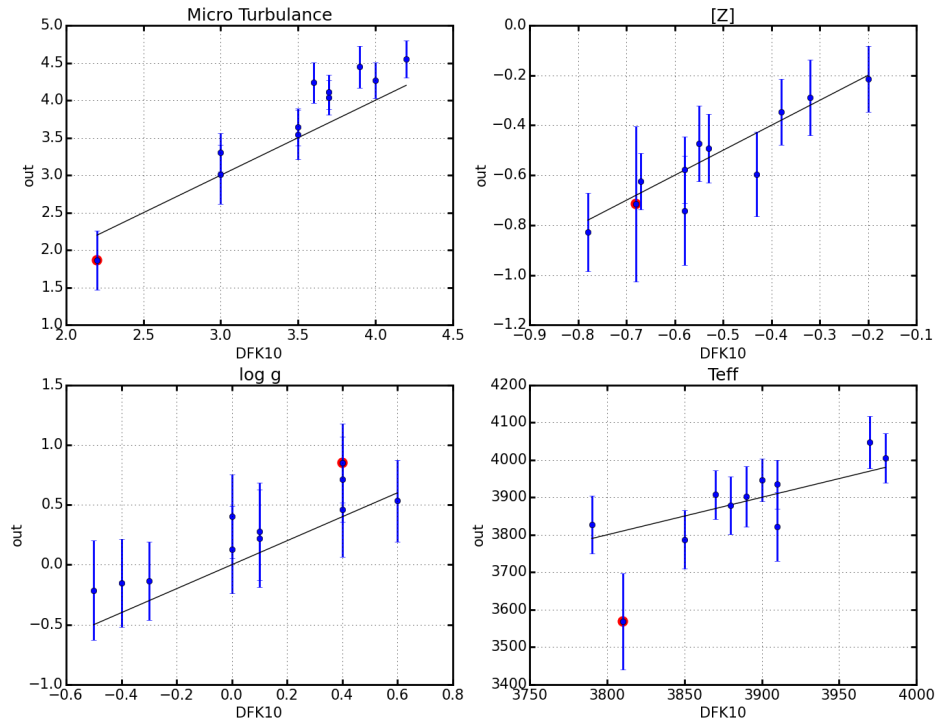


**Figure 10** *A comparison between the parameters derived for 11 RSGs in NGC 6822. DFK10 results are those published in Patrick et al. (2015).*

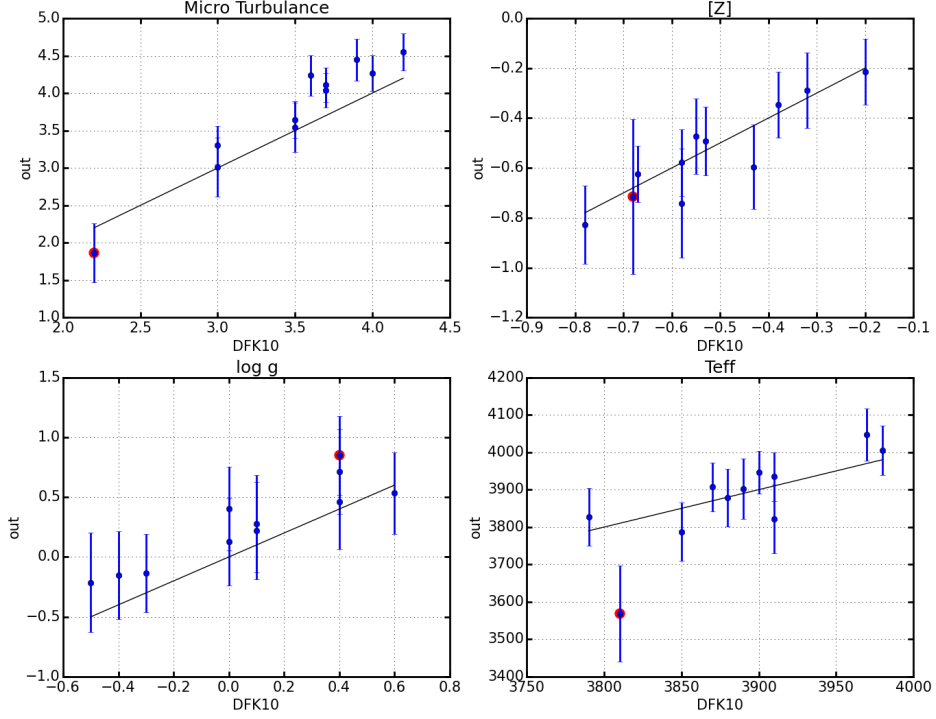


**Figure 11** *A comparison between the parameters derived for 27 RSGs in NGC 300. DFK10 results are those published in ?. Placeholder!*

implementation was set up to be complementary to that of DFK10 and was tested on high resolution spectra of RSGs in the Perseus OB-1 cluster. In addition to this, this analysis was applied to KMOS spectra of 27 RSGs of NGC 300 (?).

Stellar parameters have been derived for all spectra in NGC 300 using the presented analysis. In figure 11 I compare the results derived using the analysis presented here with those published in (?). Table 4 shows a comparison between the mean and standard deviation of the four parameters. The metallicity gradient is also derived for these observations and is found to compare ...

As part of the analysis G14 also fit for the resolution of the observations as a free parameter. The resolution for each spectrum is compared to that of the values quoted in the KMOS arc-lamp calibrations.

## 0.6 Conclusions

## References

Bergemann, M., Kudritzki, R.-P., Gazak, Z., Davies, B., and Plez, B. (2014).

**Table 4** *Average parameters for 27 RSGs in NGC300 using the G14 implementation and the implemetation discribed here **Placeholder!***

Parameter	G14 Average	Patrick Average
[Z]	$-0.52 \pm 0.16$	
$T_{eff}$	$3887 \pm 55$	
$\log g$	$0.1 \pm 0.3$	
$\xi$	$3.9 \pm 0.5$	

Red Supergiant Stars as Cosmic Abundance Probes. III. NLTE effects in J-band Magnesium lines. *ArXiv e-prints*.

Bergemann, M., Kudritzki, R.-P., Plez, B., Davies, B., Lind, K., and Gazak, Z. (2012). Red Supergiant Stars as Cosmic Abundance Probes: NLTE Effects in J-band Iron and Titanium Lines. , 751:156.

Bergemann, M., Kudritzki, R.-P., Würl, M., Plez, B., Davies, B., and Gazak, Z. (2013). Red Supergiant Stars as Cosmic Abundance Probes. II. NLTE Effects in J-band Silicon Lines. , 764:115.

Cunha, K., Sellgren, K., Smith, V. V., Ramirez, S. V., Blum, R. D., and Terndrup, D. M. (2007). Chemical Abundances of Luminous Cool Stars in the Galactic Center from High-Resolution Infrared Spectroscopy. *ApJ*, 669:1011–1023.

Davies, B., Kudritzki, R.-P., and Figer, D. F. (2010). The potential of red supergiants as extragalactic abundance probes at low spectral resolution. *MNRAS*, 407:1203–1211.

Davies, B., Kudritzki, R.-P., Gazak, Z., Plez, B., Bergemann, M., Evans, C., and Patrick, L. (2015). Red Supergiants as Cosmic Abundance Probes: The Magellanic Clouds. , 806:21.

Davies, B., Kudritzki, R.-P., Plez, B., Bergemann, M., Gazak, Z., and Evans, C. (2013). Red Supergiants as Cosmic Abundance Probes. In *EAS Publications Series*, volume 60 of *EAS Publications Series*, pages 287–292.

Davies, B., Origlia, L., Kudritzki, R.-P., Figer, D. F., Rich, R. M., and Najarro, F. (2009a). The Chemical Abundances in the Galactic Center from the Atmospheres of Red Supergiants. *ApJ*, 694:46–55.

Davies, B., Origlia, L., Kudritzki, R.-P., Figer, D. F., Rich, R. M., Najarro, F., Negueruela, I., and Clark, J. S. (2009b). Chemical Abundance Patterns in the Inner Galaxy: The Scutum Red Supergiant Clusters. *ApJ*, 696:2014–2025.

Evans, C. J., Davies, B., Kudritzki, R.-P., Puech, M., Yang, Y., Cuby, J.-G., Figer, D. F., Lehnert, M. D., Morris, S. L., and Rousset, G. (2011). Stellar metallicities beyond the Local Group: the potential of J-band spectroscopy with extremely large telescopes. *A&A*, 527:A50.



- Freytag, B., Steffen, M., and Dorch, B. (2002). Spots on the surface of Betelgeuse – Results from new 3D stellar convection models. *Astronomische Nachrichten*, 323:213–219.
- Gazak, J. K. (2014). *Red Supergiants as Luminous Beacons of Cosmic Chemical Abundances: The Infrared JBand Spectroscopic Technique*. PhD thesis, University of Hawaii.
- Gazak, J. Z., Davies, B., Kudritzki, R., Bergemann, M., and Plez, B. (2014). Quantitative Spectroscopic J-band study of Red Supergiants in Perseus OB-1. , 788:58.
- Gustafsson, B., Edvardsson, B., Eriksson, K., Jørgensen, U. G., Nordlund, Å., and Plez, B. (2008). A grid of MARCS model atmospheres for late-type stars. I. Methods and general properties. *A&A*, 486:951–970.
- Patrick, L. R., Evans, C. J., Davies, B., Kudritzki, R.-P., Gazak, J. Z., Bergemann, M., Plez, B., and Ferguson, A. M. N. (2015). Red Supergiant Stars as Cosmic Abundance Probes: KMOS Observations in NGC 6822. , 803:14.
- Plez, B. (2010). Model Atmospheres for Cool Massive Stars. In Leitherer, C., Bennett, P. D., Morris, P. W., and Van Loon, J. T., editors, *Hot and Cool: Bridging Gaps in Massive Star Evolution*, volume 425 of *Astronomical Society of the Pacific Conference Series*, page 124.
- Reetz, J. (1999). PhD thesis, LMU, Munich.
- Vílchez, J. M. and Iglesias-Páramo, J. (1998). Bidimensional Spectroscopic Mapping and Chemical Abundances of the Star-forming Dwarf Galaxy I ZW 18. , 508:248–261.